

On the origin of oldest Iron-Oxide-Copper-Gold (IOCG) deposits at the transition from Archean drip to plate tectonics

Carlos E Ganade (✉ caegeo@gmail.com)

Geological Survey of Brazil, Rio de Janeiro, Brazil

William L. Griffin

ARC Center of Excellence for Core to Crust Fluid Systems, Macquarie University, NSW 2109, Australia

Roberto F. Weinberg

Monash University, Clayton, Australia

Elena Belousova

ARC Center of Excellence for Core to Crust Fluid Systems, Macquarie University, NSW 2109, Australia

Lynthener B. Takenaka

Geological Survey of Brazil, Rio de Janeiro, Brazil

Leonardo L. Lopes

Geological Survey of Brazil, Rio de Janeiro, Brazil

Christian M. Lacasse

Geological Survey of Brazil, Rio de Janeiro, Brazil

Leandro D. Campos

Geological Survey of Brazil, Rio de Janeiro, Brazil

Research Article

Keywords: IOCG, Early Earth, Geodynamics

Posted Date: August 2nd, 2020

DOI: <https://doi.org/10.21203/rs.3.rs-50946/v1>

License: © ⓘ This work is licensed under a Creative Commons Attribution 4.0 International License.

[Read Full License](#)

Abstract

Geological evidence supports a significant change in Earth's behaviour in the mid- to late Archaean, between 3.2 and 2.5 Ga, reflecting stabilization of the lithosphere and replacement of vertical tectonics by linear imbricated belts. At the heart of this change, the oldest (c. 2.75 Ga) Iron-Oxide-Copper-Gold deposits (IOCG) were formed in the Carajás Mineral Province (CMP) of the Amazon craton. U-Pb ages, Lu-Hf isotopes and trace element composition of detrital zircons from modern drainages record the crystallization ages of the exposed rocks of the CMP. Combined with the geochemistry of Archean granitoids in the CMP, we recognize four different age and compositional groups: 3.01-2.92 Ga TTG, 2.87-2.83 Ga transitional TTG + sanukitoid + K-rich granitoids, 2.78-2.72 Ga A-type crustal granites accompanying IOCGs, and 2.59-2.53 Ga alkaline high-K intrusions accompanied by renewed IOCG mineralization. The first two groups have a dominantly juvenile isotopic signature whereas the last two have evolved Hf-isotope signatures, accompanied by increase in K_2O/Na_2O , reflecting addition of old crustal components in the melting sources over time. The older juvenile granitoids are associated with dome-and-keel structures typical of granite-greenstone terranes, whereas the younger granitoids were emplaced along a linear shear belt associated with new mafic-ultramafic intrusions and remelting of older TTG. Based on the tectono-magmatic evolution, we argue that metasomatism and fertilization of the underlying lithospheric mantle by incompatible elements, necessary for the development of IOCG deposits, were related to vertical drip-tectonics during development of the TTG proto-continent. This proto-continent made the lithosphere rigid enough to allow linear translithospheric deformation to localize at c. 2.85 Ga, allowing decompression melting of the metasomatized lithospheric mantle in a restricted extensional setting to form abundant mafic and A-type granitoids at c. 2.75 Ga, and the first IOCG deposits on Earth.

Background

The onset of plate tectonics is a heavily debated topic[1,2], but geological evidence from paleomagnetism, development of passive margins, metamorphic rocks and granitoid suggests that it was progressively established from 3.2 to 2.5 Ga[2]. Archean granitoid archives from many cratons show a change in rock chemistry between 3.2 and 2.5 Ga from intrusions of the sodic tonalite-trondhjemite-granodiorite (TTG) series to granitic intrusions with increasing potassic content[2,3,4].

The elevated Na/K, Sr/Y and high La/Yb in many TTGs is ascribed to partial melting of mafic rocks at depth, leaving a stable garnet residue[5,6]. Through time there was a decrease in TTG Na+Ca and Sr contents, which led to the distinction between high-Sr TTG (deeper, high-P melts with residual garnet) and low-Sr transitional TTG

(lower-P melts with residual plagioclase) sub-types[3,4,5,6]. Associated depletion in heavy rare earth elements

(HREE) and residual garnet requires melting of source mafic rocks in a range of 1 to 3 GPa[7,8], but depending on the source composition stability of garnet can be achieved at pressures below 1 GPa[9]. Contemporaneously with the transitional TTG, a specific and restricted type of granitoid, known as sanukitoid[10] began to appear in nearly all cratons, where they are late additions accompanied in some cases by K-rich granitoids[3]. These sanukitoids are mostly diorites to granodiorites that have a clear mantle signature, especially in their high MgO contents, but are also enriched in incompatible elements, most notably Ba and Sr, and sometimes high-field strength elements[3,4,10]. Melting experiments and petrogenetic modelling show that they may have formed either by peridotitic melting of mantle previously metasomatised by felsic melts of TTG composition, or by reaction between TTG melts and mantle[11].

Although there is no reported genetic relationship between sanukitoids and Iron Ore-Copper-Gold (IOCG) deposits, they share the same geochemical signature with enrichment in trace and minor elements typical of both basic (Co, Ni) and felsic (LREE, LILE, U, F) sources[11,12]. The source of Cu, Au, incompatible elements, and volatiles in IOCG deposits is commonly attributed to metasomatism of the underlying subcontinental lithospheric mantle (SCLM) during previous subduction events on continental margins[13,14]. Precambrian IOCG deposits occur inboard of lithospheric boundaries in necked transitions between thick Archean and thinner Proterozoic underlying mantle that focused and guided melting of this previously subduction-metasomatized mantle. In contrast, Phanerozoic IOCG deposits are preferentially located in extensional or transtensional zones of arcs[13,14]. The existence of “modern-style” subduction in the Archean is contentious[1,2,4] and the stagnant lid tectonic hypothesis is at least equally plausible to explain Archean geodynamics[15,16] and the evolving nature of Archean magmas[4]. Thus, understanding the origin and timing of Archean IOCGs and their temporal and chemical connection with the evolving Archean magmatism could help constrain the tectonic setting at the time.

The Carajás Mineral Province (CMP) of the Amazon craton in northern Brazil includes the only Archean IOCG deposit discovered so far. In this region, a long history of Archean granitoid magmatism (3.01 to 2.5 Ga) records the same compelling change in rock chemistry reported in other cratons[3]. Here we report on ages, Hf isotopic composition and trace elements of zircons from modern drainages within the CMP, which reflect the nature of the exposed Archean rocks. We combine these results with available zircon crystallization ages and bulk-rock chemistry of granitoids to define a temporal evolution linked to the tectonic evolution of the region. We argue that emplacement of the 2.87-2.83 Ga transitional TTG and sanukitoid magmas records early fertilization and melting of the lithospheric mantle, which was re-melted at c. 2.75 Ga to generate the IOCG mineral systems in the transition from drip to mobile tectonics in the Amazon Craton. This differs from the models of mantle enrichment via subduction proposed for the younger IOCGs[12].

GEOLOGICAL SETTING OF CARAJÁS MINERAL PROVINCE (CMP) AND ITS IOCG DEPOSITS

The CMP region encompasses three main rock associations: i) Archean basement rocks (3.00-2.83 Ga) represented by TTG-greenstone belt associations, with minor sanukitoids and K-rich granitoids[17,18,19,20]; ii) the Carajás basin composed of a meta-volcanosedimentary sequence,

including thick Superior-type BIFs coeval with the intrusion of A-type granitoids and layered mafic-ultramafic complexes (2.78-2.72 Ga), alkaline high-K intrusions (c. 2.56 Ga) and younger low-grade siliciclastic cover rocks[21,22]; and iii) widespread Paleoproterozoic (c. 1.88 Ga) A-type intrusions[23] (Fig. 1). To the north, these lithologies are bounded by high-grade rocks (gneisses and migmatites) of Paleoproterozoic age (2.50-1.96 Ga) within older Archean terranes. Interpretations based on geological, bulk-rock geochemistry and isotopic data have led to two contrasting interpretations for the tectonic setting of the Carajás Basin: an intracontinental rift forming the Carajás basin[21,22] or a compressional arc-related setting[24].

In the CMP, the region to the south of the Carajás basin, the environment related to the emplacement of the

3.0 to 2.83 Ga TTGs is preserved, with the dome-and-keel structures typical of many granite-greenstone terranes[25] such as the Mogno dome[26,27] in Fig. 1. The dome-and-keel terrane is bound to the north by a high- to low grade 200-km wide anastomosing set of E-W to ESE-WNW strike-slip shear zones and faults (Itacaiúnas shear belt) developed around 2.85 Ga. This shear belt was later reactivated by sinistral motion at the time of development of Carajás basin at 2.78-2.72 Ga, accompanied by the intrusion of syn-kinematic A-type granites[20,28,29].

The IOCG deposits are located along or near these reactivated shear zones, in proximity to intrusions of different compositions, and are characterized by Fe-oxides and enrichment in Cu-Au-REE-(U-Y-Ni-Co-Pd-Sn-Bi-Pb-Ag-Te)[27]. They have been affected by intense proximal K-Fe and distal Na-Ca hydrothermal alteration with late-stage chlorite and carbonates, associated with hypersaline fluids (250°-570°C) and late sulphide deposition with different sulfidation states[30]. Geochronology points to two main IOCG mineralization events at 2.75-2.68 Ga and 2.62-2.50 Ga[31], the first associated with reactivated regional shear zones and syn-kinematic intrusions of A-type granitoids[20] and the later to a second reactivation stage accompanied by minor alkaline high-K granitoids[32].

Results

Detrital zircons from modern drainages in the CMP have either oscillatory zoning or are homogeneous in CL images, indicating that they crystallized from magmas (Fig. 2A). However, some zircons are rounded to ovoid and show core-mantle relationships. Their $^{207}\text{Pb}/^{206}\text{Pb}$ ages define four distinct groups (G1 to G4) that correspond to the zircon U-Pb and Pb-Pb crystallization ages of the exposed rocks, and hence they record peaks in magma addition into the CMP crust (Fig. 2B and supplementary table S1). Peaks in magmatism, from G1 to G4, occurred at 3.05-2.92, 2.87-2.83, 2.78-2.72, and 2.59-2.53 Ga. In general, and based on the known regional geology, they are associated with an evolution from Na-rich high-HREE TTGs (G1) grading into low-HREE TTGs and MgO-rich sanukitoids (G2), and then to high-K granitoids (G3), revealing an enrichment in K over Na throughout time (Fig. 2C and D). Trace-element discriminants (Y, Hf, U, Th, Yb and Lu) used to infer the zircon host rock during crystallization[33] points to a dominance of granitoid sources with important mafic addition in G3, during the development of Carajás basin. Three

zircon grains suggest crystallization from a carbonatites or other highly alkaline rocks. The evolving granitoid chemistry is accompanied by a trend in zircon Hf isotope ratios from the early radiogenic juvenile signature of TTG rocks of G1 group ($eHf_{(t)} = +1.13$ to $+6.56$) to progressively evolved and less radiogenic values where G2 has $eHf_{(t)} = -5.31$ to $+6.76$, G3 has $eHf_{(t)} = -6.83$ to $+1.19$ and G4 has $eHf_{(t)} = -4.41$ to $+8.27$ (Fig. 2B). Hf model ages for the younger G2, G3 and G4 magmatism varies from 3.28 to 3.01 Ga which overlaps with the U-Pb and Hf model ages of G1.

Discussion

As mentioned, in general, the enrichment in K over Na is marked by the transition from TTG to K-rich granitoids, reflecting the increased importance of crustal components in the melt sources, indicated by the trend in zircon Hf isotope ratios (Figs. 2 and 3A). The TTGs of G1 and G2 show a wide range of Sr/Y and Eu*, suggesting that both garnet-rich and plagioclase-rich residues were involved, while G3 granitoids have lower Sr/Y (Figs. 3B and C) However, an increase in Sr/Y and (La/Yb)_N during G1 (3.05-2.92 Ga) TTG magmatism (3B) indicates a deepening of the melt source[5] towards G2 associated transitional TTGs. This shift is also captured by the overall development of a positive Eu anomaly over the same interval, reflecting the increasing presence deeper plagioclase-free residues from G1 to G3 (Fig. 3D). The T_{DM} ages of all the igneous zircons coincide between 3.25 and 2.90 Ga, indicating that they could be generated by reworking G1 juvenile TTG or rocks with similar isotopic signature.

The dome-and-keel geometry preserved in the south CMP region preserved in the Mogno dome (Fig. 1) shows that vertical tectonics played an important role during granitoid emplacement from 3.01 to 2.83 Ga. In the absence of Archean “modern-style” subduction[1,2,4], crustal tectonics could be driven by forces related to mantle convection under a cold lithospheric lid[34]. Numerical models indicate that this process creates lithospheric drips where mantle convection cells downwell and is an efficient way to drag crustal rocks deep into the mantle, where they can melt at high pressures[34]. Models also have shown that drips can evolve from symmetric (vertical) to asymmetric (tilted), mimicking “modern-style” subduction zones with important implications for the melts arising from the drips[4]. We use these drip models to interpret the evolution of magmatism in the CMP and the origin of its IOCGs.

We propose that during the 3.00-2.92 Ga magmatism in the CMP region is associated with the development of a symmetric drip dragging down crustal mafic rocks from the lid causing melting, below the garnet-in isograd, to form the juvenile G1 TTG melts (Fig. 4A). Lateral displacement of the lid due convection led the drip to become asymmetric starting the G2 magmatic stage. At this stage, previously-formed TTGs were dragged down by the drip and re-melted in conjunction with the melting of mafic rocks[4], forming transitional TTGs and accounting for the increased K content of the G2 granitoids between 2.87-2.83 Ga. Recycling of older crustal rocks is reflected in their Hf isotopic values. The increase in Sr/Y values along with the positive Eu anomaly from G1 to G2 reflects the deepening of melt source in a transition from symmetric to asymmetric dripping. Because of this drip asymmetry new TTG magmas rose through and metasomatized the lithospheric mantle wedge (Fig. 4B) enriching it in LREE, LILE and some HFSE[4]. The contemporaneous dehydration[4] and release of fluids from the tilted mafic crustal drip

could also trigger partial melting of this metasomatized mantle wedge, generating the high-Mg sanukitoid rocks observed in the 2.87-2.83 Ga interval (G2). The ascent of these hot G2 sanukitoid magmas would then favour melting of older TTG crust, generating the coeval high-K granitoids (Fig.4B) with ancient T_{DM} model ages.

Enrichment of the mantle in LILE, REE and Cl has been attributed to fertilization by aqueous fluids from dehydrating oceanic plates[35]. The same 'subduction' effect would be expected from the dehydration of the crustal mafic lid in the asymmetric drip phase, arguably responsible for the metasomatism of the lithospheric mantle associated to the sanukitoid magmatism in the 2.87-2.83 Ga interval. On the other hand, metasomatism of the mantle wedge above the drip would also be achieved through fluid-free processes by the interaction of felsic TTG melts with mantle peridotites[11]. The role of mantle fluids in IOCG deposits has been demonstrated by the positive $\delta^{37}\text{Cl}$ values (+0.2 to +2.1‰) derived from fluid inclusions from selected deposits, including the Sossego deposit of the CMP[36].

The development of linear belts in the CMP region started during late G2 magmatism, with the nucleation of the Itacaiúnas shear belt at 2.85 Ga[28] along with metamorphism[37] and emplacement of G2 2.85-2.83 Ga sanukitoids and high-K granitoids along the shear belt[19]. This stage indicates that the proto-continent formed by the older TTGs of G1 and G2 was rigid enough to allow strain localization and linear deformation, arguably associated to far-field stresses resulting from the development of an Archean orogens elsewhere.

Continuous far-field stresses reactivated earlier structures during G3 magmatism at 2.78-2.72 Ga, developing the localized transtensional Carajás rift basin[29]. These structures could have reached the base of the lithosphere[38], and extension would have promoted heating and decompressional partial melting of the drip- metasomatized mantle (Fig. 4C). Comparison of empirical melting relations with modelled P-T conditions in the lithosphere during extension indicates that large volumes of magma may be produced by decompressional partial melting of melt-metasomatized mantle during the earliest stages of extension in localized rift basins[39,40]. These melts would pond at the base of the Itacaiúnas shear belt and ascend to generate the mafic-ultramafic rocks of the CMP and the Carajás basin, while the heat transferred by such underplating would favour melting at the base of the previous TTG proto-continent, yielding coeval syn-kinematic[20] A-type granites with ancient Hf-isotope signatures. Transport of the Cu and REE to into IOCG mineralization is commonly attained by chloride complexes[41,42]. We argue that the Itacaiúnas shear belt and its successive reactivated structures acted as conduits connecting the mantle to the upper crustal levels of the CMP. This event along the translithospheric shear zones of the Itacaiúnas shear belt would be volatile-rich[43] and able to transfer the Cu, REE and LILE from the drip-metasomatized mantle to shallow crustal levels where mixing with the basinal brines[30] allow the breakdown of the chloride complexes and deposition of the first pulse of Cu endowment in the CMP at *c.* 2.76 Ga.

The last magmatic event at 2.59-2.53 Ga (G4) is marked by granitoids with exclusively evolved zircon Hf signatures, which suggests yet another reactivation event. This reactivation is corroborated by the partial

or total resetting of the U-Pb and Rb-Sr systems and by Ar-Ar cooling ages together with the third pulse of IOCG mineralization at 2.60-2.45 Ga[31,44]. This magmatic event includes also minor high-K alkaline intrusions related to the sinistral reactivation of the northern shear zones of the CMP[28,32,37]. During this reactivation minor partial melting of the drip-metasomatized mantle tapped by the lithospheric shear zones, accompanied by volatile-rich batches, could produce both the alkaline incompatible-element-rich magmatism and renewed IOCG mineralization.

We present here an evolutionary history of the granitoid archive of the CMP where we integrate the origin of the IOCGs, where both magmas and mineralization inform on the tectonic setting and mantle alteration processes. In this evolution, we use published numerical models for Archean geodynamics to argue that that no subduction is necessary to explain the genesis of magmatic rocks from 3.01 to 2.50 Ga and that enrichment of the mantle, a necessary ingredient for IOCG mineralization, could be attained through drip tectonics[4]. The Hf-isotope record demonstrates that after a period of crustal growth ending at *c.* 2.9 Ga, the crust evolved through progressive reworking of the oldest rocks to produce younger generations of granitoids, a process that would be favoured by an essentially in-situ mechanism such as drip tectonics. The early TTGs were part of a broader process that formed this increasingly rigid proto-continent, and allowed strain localization into linear shear belts that were later reactivated to form narrow extensional rift zones connected by shear zones to the underlying lithospheric mantle. Decompression melting by mantle upwelling during rifting from 2.78-2.72 Ga was responsible for concentrated mafic-felsic activity in the rift zone and first Earth's IOCG deposits tapping the fluids in the metasomatized lithospheric mantle. This event was followed by reactivation of the process at 2.59-2.53 Ga aided by volatiles from the mantle, promoting renewed IOCG mineralization in the CMP.

Methods

Sampling and data compilation. Four samples from modern drainages of the Carajás Mineral Province were collected on the Rio Plaque (sample BA236432), Rancho Refugio Drainage (sample BA236438), Rio Novo Drainage (sample BA236443) and Rio Sereno drainage (sample BA236447). For sample locations see Figure 1. Data are reported in the supplementary table S1. In order to strength interpretation on detrital zircon data we have extensively compiled whole-rock geochemistry and zircon U-Pb and Pb-Pb ages from Archean rocks of Carajás Mineral Province region. The compiled data is reported in the supplementary table S2.

Major and Trace Element Determinations. The major constituents of zircon, Zr and Si, and selected minor elements such as Hf, Y, U and Th were analysed using GEMOC's CAMEBAX SX50 electron microprobe. More precise Uranium and Thorium concentrations were calculated from LAM-ICPMS U-Th-Pb analyses by comparison of U and Th raw counts with those obtained for the GEMOC GJ1 standard. Yb/Hf and Lu/Hf ratios collected as part of the multi-collector ICPMS Hf-isotope analysis were converted to Yb and Lu concentrations using the Hf contents determined by electron microprobe. All grains were imaged using

back-scattered electrons in a Zeiss Scanning Electron Microprobe to provide maps for the selection of appropriate spots for U-Pb and Lu-Hf analyses.

Zircon U-Pb dating. The zircon grains were mounted in epoxy discs and polished. Grain mounts containing the samples and zircon standards were cleaned in 2N nitric acid for *ca.* 1 hour prior to analysis. Analyses were performed using a custom built UV LAM [46] coupled to an Agilent 4500, series 300, ICPMS at the GEMOC Key Centre, Macquarie University. Samples and standard were ablated in a custom-built sample chamber using He to carry ablated material out of the sample cell and into the ICPMS. Relative to ablation in Ar, ablation in He minimises deposition of ablation products around ablation sites, improves sample transport efficiency, results in more stable signals and gives more reproducible Pb/U fractionation. To minimise dynamic U/Pb fractionation as the laser beam penetrates into the sample [47] all analyses were performed with the laser focused above the sample (typically ~ 200 μm). Identical laser operating conditions (laser energy and degree of defocusing) were rigorously maintained throughout each run of 20 analyses to ensure constant U/Pb fractionation. It should be noted that the effect of any uncorrected U-Pb fractionation is to move data points along a chord corresponding to zero-age Pb loss or gain in the concordia plot, without affecting the $^{207}\text{Pb}/^{206}\text{Pb}$ ages. Ablation pit diameter was generally 40-50 μm . Samples were analysed in separate "runs" of 20 analyses comprising 12 analyses of unknowns bracketed, before and after, by 4 analyses of the GEMOC GJ-1 zircon standard, a gem quality zircon believed to be from an African pegmatite. Each analysis took ~180 seconds, with gas background measurements being taken over the first ~60 seconds, prior to initiation of ablation. Data were acquired on five isotopes using the instrument's time-resolved analysis data acquisition software with short dwell times to provide quasi- simultaneous measurement of the five masses and optimum precision. ^{204}Pb was not determined due to low count rates and the isobaric interference from Hg, which is a significant contaminant in the Ar supply gas. The time-resolved analysis software determines signal intensity data for each mass sweep performed by the mass spectrometer. Time-resolved signals (*i.e.*, signals as a function of time, which is a proxy for ablation depth) generally allow isotopic heterogeneity within the ablation volume to be clearly identified (*e.g.*, zones of Pb loss or common Pb related to fractures or areas of radiation damage; also inclusions, inherited cores, *etc.*). Raw data were processed using GLITTER, an in-house on-line data reduction program. $^{207}\text{Pb}/^{206}\text{Pb}$, $^{208}\text{Pb}/^{232}\text{U}$, $^{206}\text{Pb}/^{238}\text{U}$ and $^{207}\text{Pb}/^{235}\text{U}$ ($^{235}\text{U} = ^{238}\text{U}/137.88$) ratios were calculated for each mass sweep and the time-resolved ratios for each analysis were then carefully examined. Optimal signal intervals for the background and ablation data were selected for each sample and automatically matched with identical time intervals for the standard zircon analyses, thus correcting for the effects of ablation/transport-related U/Pb fractionation and mass bias of the mass spectrometer. Net background-corrected count rates for each isotope were used for calculation of sample ages. The data in the result Tables show internal precision (1s) based on counting statistics on standards and sample. Concordia ages were determined using Isoplot 2.32[48]. To monitor the quality of the data obtained with this technique, analyses of well-characterised zircons such as the Mud Tank zircon 734 ± 32 Ma[49] and 91500 1064 Ma[50], have been run within each set separate "run" of 20 analyses. The U-Pb age data obtained for Mud

Tank and 91500 zircon during this project are given by comparison with TIMS data. *Common-Lead Correction:* Traditionally, common-lead is measured by analysis of ^{204}Pb , and the isotopic composition of lead corrected accordingly. However, LAM-ICPMS U-Pb analyses do not report ^{204}Pb , because of the low peak/background ratio of the ^{204}Pb peak due to the presence of Hg in the argon nebuliser gas. An alternative approach to common-lead correction of U-Pb data proposed by [51] neither requires knowledge of the amount of ^{204}Pb present, nor assumes that corrected compositions plot on the concordia. Assuming that the observed discordance due to a combination of (1) *lead-loss at a given time t_L* and (2) *contamination by common-lead of known composition*, the common-lead component is removed by stepwise subtraction of common $^{206}\text{Pb}_c$, $^{207}\text{Pb}_c$ and $^{208}\text{Pb}_c$ from the observed composition, until the residual composition matches the isotopic pattern of a lead which has only suffered lead-loss. The procedure allows the simultaneous determination of the amount of common-lead present and the corrected $^{206}\text{Pb}_r/^{238}\text{U}$, $^{207}\text{Pb}_r/^{235}\text{U}$ and $^{208}\text{Pb}_r/^{232}\text{Th}$ ratios. This method is thus applicable to U-Pb analyses which do not report ^{204}Pb , or do so only with inferior precision, and to grains which have suffered lead-loss in addition to contamination by common-lead. A more detailed description of the correction methodology is given by ref. [51].

Hf Isotope Determination. Hf isotope data for the same set of zircons were collected as described by ref [52]. Hf isotope analyses were carried out *in situ* with a Merchantek EO LUV 266nm laser-ablation microprobe, attached to a Nu Plasma multi-collector ICPMS at GEMOC, Macquarie University, Sydney. Most analyses were carried out with a beam diameter of 60-80 μm , a 10 Hz repetition rate, and energies of 0.6-1.3 mJ/pulse. Typical ablation times were 80-120 s, resulting in pits 40-60 μm deep. The methodology and analyses of standard solutions and standard zircons are described by ref. 7. Masses 172, 175, 176, 177, 178, 179 and 180 were analysed simultaneously in Faraday cups; all analyses were carried out in static-collection mode. Data were normalised to $^{179}\text{Hf}/^{177}\text{Hf} = 0.7325$, using an exponential correction for mass bias. Interference of ^{176}Lu on ^{176}Hf is small and was corrected using the recommended $^{176}\text{Lu}/^{175}\text{Lu} = 0.02669$. Interference of ^{176}Yb on ^{176}Hf was corrected using $^{176}\text{Yb}/^{172}\text{Yb} = 0.5865$; this value was determined by successive spiking of the JMC475 Hf standard (1 ppm solution) with Yb, and iteratively finding the value of $^{176}\text{Yb}/^{172}\text{Yb}$ required to yield the value of $^{176}\text{Hf}/^{177}\text{Hf}$ obtained on the pure Hf solution. Excellent precision and accuracy are obtainable even with large corrections on ^{176}Hf [7]. All laser-ablation analyses were carried out using time-resolved data acquisition mode, in which the signal for each mass and each ratio is displayed as a function of time during the analysis. This allows the more stable portions of the ablation to be selected for integration, before the data are processed to give the final results. Background was collected on peak for 45 seconds before ablation was initiated

Declarations

ACKNOWLEDGMENTS

CEG acknowledges the Center of Technological Development of the Geological Survey of Brazil for the support in this research. Part of this discussion was initially presented by CEG in December 2015 during an internal CMP workshop of the Geological Survey of Brazil, held in the city of Belem, and benefited from estimated recent advances in geodynamics numerical modelling by several authors.

AUTHOR CONTRIBUTIONS

CEG, WLG and RW conceived the idea and wrote the paper. WLG and EB acquired the zircon U-Pb, Hf and trace element data. CEG and LBT assisted in the zircon U-Pb/Pb-Pb data compilation and organization. CEG, LLL, CML and LDC assisted in the whole-rock geochemical data compilation and organization.

ADDITIONAL INFORMATION

Competing interests: The authors declare no competing interests.

References

1. Korenaga, J. Initiation and evolution of plate tectonics on Earth: theories and observations. *Rev. Earth Planet. Sci.* 41, 117-151 (2013).
2. Cawood, P. A. *et al.* Geological archive of the onset of plate tectonics. *Trans. R. Soc.: Math., Phys. and Eng. Sci.* 376(2132), 20170405 (2018).
3. Laurent, , Martin, H., Moyen, J. F. & Doucelance, R. The diversity and evolution of late-Archean granitoids: evidence for the onset of 'modern-style' plate tectonics between 3.0 and 2.5 Ga. *Lithos* 205, 208-235 (2014)
4. Nebel, O. *et al.* When crust comes of age: on the chemical evolution of Archaean, felsic continental crust by crustal drip tectonics. *Trans. R. Soc.: Math., Phys. and Eng. Sci.* 376(2132), 20180103 (2018)

5. Moyen, J. F., Champion, D. & Smithies, R. H. The geochemistry of Archaean plagioclase-rich granites as a marker of source enrichment and depth of melting. *Earth Environ. Sci. Trans. R. Soc. Edinburgh* 100, 35-50 (2010).
6. Martin, H. & Moyen, J. F. Secular changes in tonalite-trondhjemite-granodiorite composition as markers of the progressive cooling of Earth. *Geology* 30, 319-322 (2002).
7. Zhang, C, et al. Constraints from experimental melting of amphibolite on the depth of formation of garnet- rich restites, and implications for models of Early Archean crustal *Precam. Res.* 231, 206-217 (2013).
8. Rapp, P., Shimizu, N., Norman, M.D. Growth of early continental crust by partial melting of eclogite. *Nature* 425, 605-609 (2003).
9. Palin, R. M., White, R. W., Green, E. C. R. Partial melting of metabasic rocks and the generation of tonalitic- trondhjemitic-granodioritic (TTG) crust in the Archaean: constraints from phase equilibrium *Precam. Res* 287, 73-90 (2016).
10. Shirey, S.B. & Hanson, G.N. Mantle-derived Archean monzodiorites and trachyandesites. *Nature* 310, 222- 224 (1984).
11. Martin, H., Moyen, J. F. & Rapp, R. The sanukitoid series: magmatism at the Archaean–Proterozoic transition. *Earth Environ. Sci. Trans. R. Soc. Edinburgh* 100(1-2), 15-33 (2009).
12. Groves, I., Bierlein, F. P., Meinert, L. D. & Hitzman, M. W. Iron oxide copper-gold (IOCG) deposits through Earth history: Implications for origin, lithospheric setting, and distinction from other epigenetic iron oxide deposits. *Econ. Geol.* 105(3), 641-654 (2010).

13. Groves, I., Vielreicher, R. M., Goldfarb, R. J. & Condie, K. C. Controls on the heterogeneous distribution of mineral deposits through time, *in* Mc Donald, I. et al., eds., *Mineral Deposits and Earth Evolution: Geol. Soc. London, Spec. Publ.* 248, 71-101 (2005).
14. Kerrich, R., Goldfarb, R. J. & Richards, J. P. Metallogenic provinces in an evolving dynamic framework. *Geol. 100th Anniv. Vol.*, 1097–1136 (2005).
15. Rozel, A. B., Golabek, G. J., Jain, C., Tackley, P. J. & Gerya, T. Continental crust formation on early Earth controlled by intrusive magmatism. *Nature* 545, 332-335 (2017).
16. O'Neill, C., Turner, S., & Rushmer, T. The inception of plate tectonics: a record of failure. *Trans. R. Soc.: Math., Phys. and Eng. Sci.*, 376(2132), 20170414 (2018).
17. Macambira, B. & Lancelot, J. R. Time constraints for the formation of the Archean Rio Maria crust, southeastern Amazonian Craton, Brazil. *Geol. Rev.* 38, 1134-1142 (1996).
18. Oliveira, M. A., Dall'Agnol, R. & Almeida J. A. C. Petrology of the Mesoarchean Rio Maria suite and the discrimination of sanukitoid series. *Lithos* 127, 92–209 (2011).
19. Feio, G. R. L. *et al.* Archean granitoid magmatism in the Canaã dos Carajás area: Implications for crustal evolution of the Carajás province, Amazonian craton, Brazil. *Res.* 227, 157-185 (2013).
20. Marangoanha, B., Oliveira, D. C., Oliveira, V. E. S., Galarza, M. A. & Lamarão, C. N. Neoproterozoic A-type granitoids from Carajás province (Brazil): New insights from geochemistry, geochronology and microstructural analysis. *Res.* 324, 86-108 (2019).
21. Gibbs, A. K., Wirth, K. R., Hirata, W. K. & Olszewski Jr., W. J. Age and composition of the Grão Pará Group volcanics, Serra dos Carajás. *Brazilian Jour. Geosci.* 16, 201-211 (1986).

22. Grainger, J., Groves, D. I., Tallarico, F. H. B. & Fletcher, I. R. Metallogensis of the carajás mineral province, southern Amazon Craton, Brazil: Varying styles of Archean through Paleoproterozoic to Neoproterozoic base- and precious-metal mineralization. *Ore Geol. Rev.* 33, 451-489 (2008).
23. Tallarico, F. H. B. et al. Geological and SHRIMP II U-Pb constraints on the age and origin of the Breves Cu- Au-(W-Bi-Sn) deposit Carajás, Brazil. *Depos.* 39, 68-86 (2014).
24. Meirelles, M. R. & Dardenne, M. A. Vulcanismo basáltico de afinidade shoshonítica em ambiente de arco arqueano, Grupo Grão-Pará, Serra dos Carajás – Pará (*in portuguese*). *Brazilian Geosci.* 21, 41-50 (1991).
25. Zibra, I. et al. Regional-scale polydiapirism predating the Neoproterozoic Yilgarn Orogeny. *Tectonophysics* 779, 228375 (2020).
26. Lacasse, C. et al. Restoring original composition of hydrothermally altered Archean metavolcanic rocks of the Carajás Mineral Province (Brazil): geodynamic implications for the transition from lid to mobile tectonics. *Lithos* 370-371, 105647 (2020).
27. Costa, F. G., Santos, P. A. & Silva, C. M. G. Change from dome-and-keel architecture to "modern-style" tectonics in the Carajás Province, (*conference abstract*) *16th Simpósio de Geologia da Amazônia*, Manaus (2020).
28. Pinheiro, R. V. L. & Holdsworth, R. E. Reactivation of Archaean strike-slip fault systems, Amazon region, Brazil. *Soc. London* 154, 99-103 (1997).
29. Holdsworth, E. & Pinheiro, R.V.L. The anatomy of shallow-crustal transpressional structures: insights from the Archaean Carajás fault zone Amazon, Brazil. *Jour. Struct. Geol.* 22, 1105-1123 (2000).

30. Xavier, P. et al. The iron oxide copper-gold systems of the Carajás mineral province, Brazil. *Econ. Geol.* 16, 433-453 (2012).
31. Trunfull, E. F., Hagemann, S. G., Xavier, R. P. & Moreto, C. P. Critical assessment of geochronological data from the Carajás Mineral Province, Brazil: implications for metallogeny and tectonic evolution. *Ore Geol. Rev.* 121, 103556 (2020).
32. de Freitas Toledo, I., Moreto, C. P. N., Xavier, R. P., Gao, J. & de Melo, G. H. C. Multistage Evolution of the Neoproterozoic (ca. 2.7 Ga) Igarapé Cinzento (GT-46) Iron Oxide Copper-Gold Deposit, Cinzento Shear Zone, Carajás Province, Brazil. *Econ. Geol.* 114(1), 1-34 (2019).
33. Belousova, E., Griffin, W.L., O'Reilly, S.Y. & Fisher, N.L. Igneous zircon: trace element composition as an indicator of source rock type. *Miner. and Petrol.* 143(5), 602-622 (2002).
34. Capitanio, F. A., Nebel, O., Cawood, P. A., Weinberg, R. F. & Clos, F. Lithosphere differentiation in the early Earth controls Archean tectonics. *Earth and Planet. Sci. Lett.* 525, 115-755 (2019).
35. Kawamoto, T et al. Large-ion lithophile elements delivered by saline fluids to the sub-arc mantle. *Earth, Planets and Space* 66(1), 61 (2014).
36. Chiaradia, M., Banks, D., Cliff, R., Marschik, R. & De Haller, A. Origin of fluids in iron oxide–copper–gold deposits: constraints from $\delta^{37}\text{Cl}$, $^{87}\text{Sr}/^{86}\text{Sr}$ and Cl/Br. *Depos.* 41(6), 565-573 (2006).
37. Machado, N., Lindenmayer, Z., Krogh, T.E. & Lindenmayer, D. U-Pb geochronology of Archean magmatism and basement reactivation in the Carajás area Amazon shield, Brazil. *Res.* 49, 329-354 (1991).
38. Petrunin, A. & Sobolev, S. V. What controls thickness of sediments and lithospheric deformation at a pull- apart basin? *Geology* 34, 389-392 (2006).

39. Harry, D. L. & Leeman, W.P. Partial melting of melt metasomatized subcontinental mantle and the magma source potential of the lower *Jour. of Geophys. Res.: Solid Earth* 100(B6), 10255-10269 (1995).
40. Rychert, C. A. et al. Volcanism in the Afar Rift sustained by decompression melting with minimal plume influence. *Geosci.* 5(6), 406-409 (2012).
41. Smith, P., Gleeson, S. A. & Yardley, B.W.D. Hydrothermal fluid evolution and metal transport in the Kiruna District, Sweden: Contrasting metal behaviour in aqueous and aqueous-carbonic brines. *Geoch. et Cosmoch. Acta* 102, 89-112 (2013).
42. Williams-Jones, A.E. & Heinrich, C.A, Vapor transport of metals and the formation of magmatic-hydrothermal ore deposits. 100th Anniversary special paper: *Geol.* 100(7), 1287-1312 (2005).
43. McCaig, M. The geochemistry of volatile fluid flow in shear zones. *Mineral. Soc. Ser. 8*, 227-266 (1997).
44. Pollard, P. J et al. ⁴⁰Ar-³⁹Ar dating of Archean iron oxide Cu-Au and Paleoproterozoic granite-related Cu-Au deposits in the Carajás Mineral Province, Brazil: implications for genetic models. *Depos.* 54(3), 329-346 (2019).
45. Smithies, H. The Archaean tonalite-trondhjemite-granodiorite (TTG) series is not an analogue of Cenozoic adakite. *Earth Planet. Sci. Lett.* 182, 115-125 (2000).
46. Profeta, et al. Quantifying crustal thickness over time in magmatic arcs. *Scientific reports* 5, 17786 (2015).
46. Norman, D., Pearson, N. J., Sharma, A. & Griffin, W. L. Quantitative analysis of trace elements in geological materials by laser ablation ICPMS: instrumental operating conditions and calibration

- values of NIST glasses. *Geostand. Newslett.* 20(2), 247-261 (1996).
47. Hirata, T. & Nesbitt, R. W. U-Pb isotope geochronology of zircon: Evaluation of the laser probe-inductively coupled plasma mass spectrometry technique. *et Cosmoch. Acta* 59(12), 2491-2500 (1995).
48. Ludwig, K. R. Isoplot/Ex version 3.0. A geochronological toolkit for Microsoft Excel (Berkeley *Geochronological Centre Spec. Pub.*, (2003).
49. Black, P., & Gulson, B. L. The age of the Mud Tank Carbonatite, Strangways Range, Northern Territory. *Jour. of Australian Geol. & Geoph.* 3, 227-232 (1978).
50. Wiedenbeck, M., Alle, P., Corfu, F., Griffin, W.L., Meier, M., Oberli, F., Von Quadt, A., Roddick, J.C., Spiegel, (1995). Three natural zircon standards for U–Th–Pb, Lu–Hf, trace element and REE analyses *Geostand. Newslett.* 19, 1-24.
51. Andersen, T. Correction of common lead in U–Pb analyses that do not report ^{204}Pb . *Geol.* 192(1-2), 59-79 (2002).
52. Griffin, W. L., Pearson, N. J., Belousova, E., Jackson, S. V., Van Acherbergh, E., O'Reilly, S. Y., Shee, S. R. The Hf isotope composition of cratonic mantle: LAM-MC-ICPMS analysis of zircon megacrysts in kimberlites. *et Cosmoch. Acta* 64(1), 133-147 (2000).

Figures

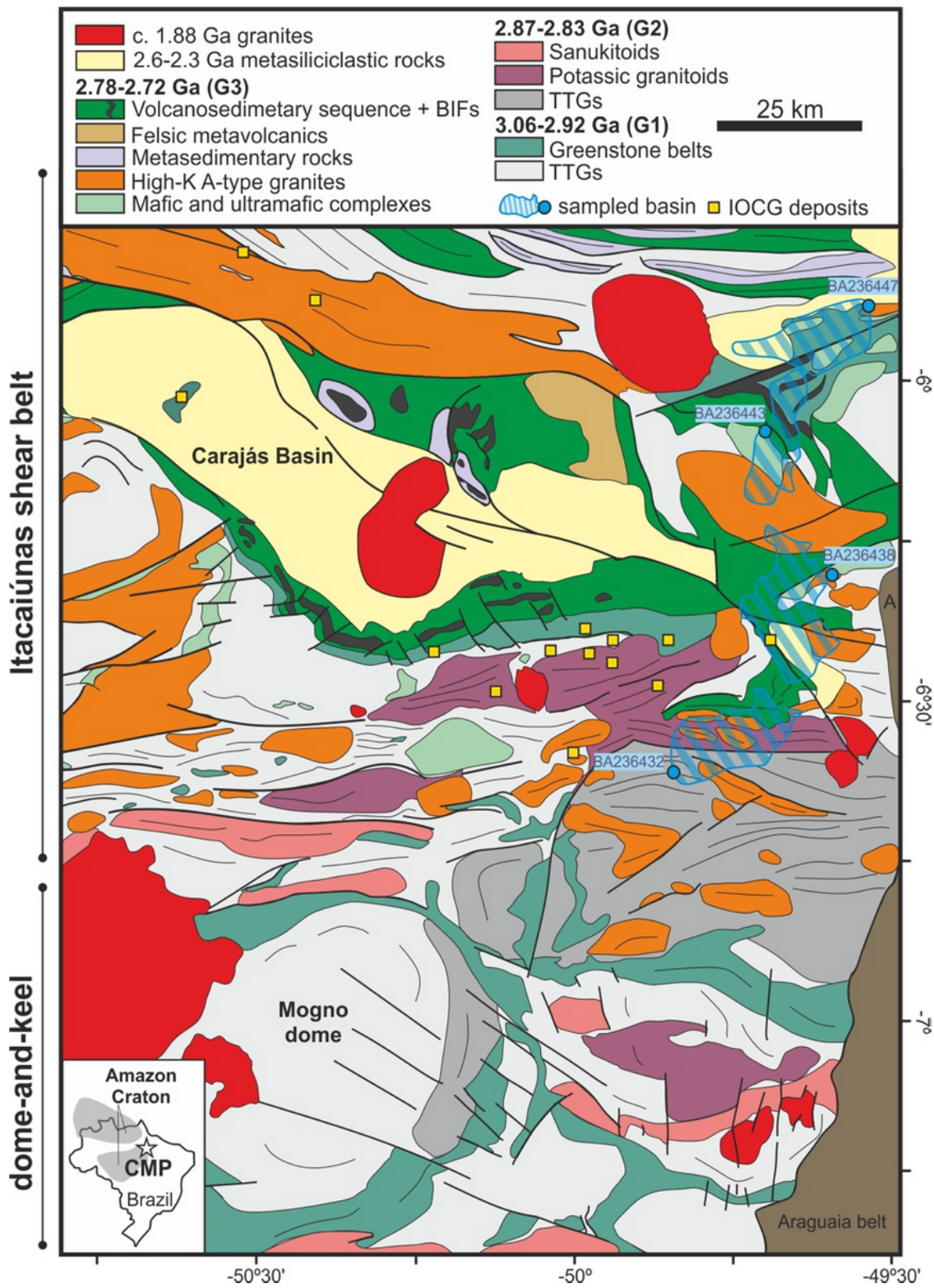


Figure 1

Geological context of CMP region granitoids, shear zones and IOCG deposits. Simplified geological map modified from refs. [18,26]. Location of IOCG deposits after ref. [30].

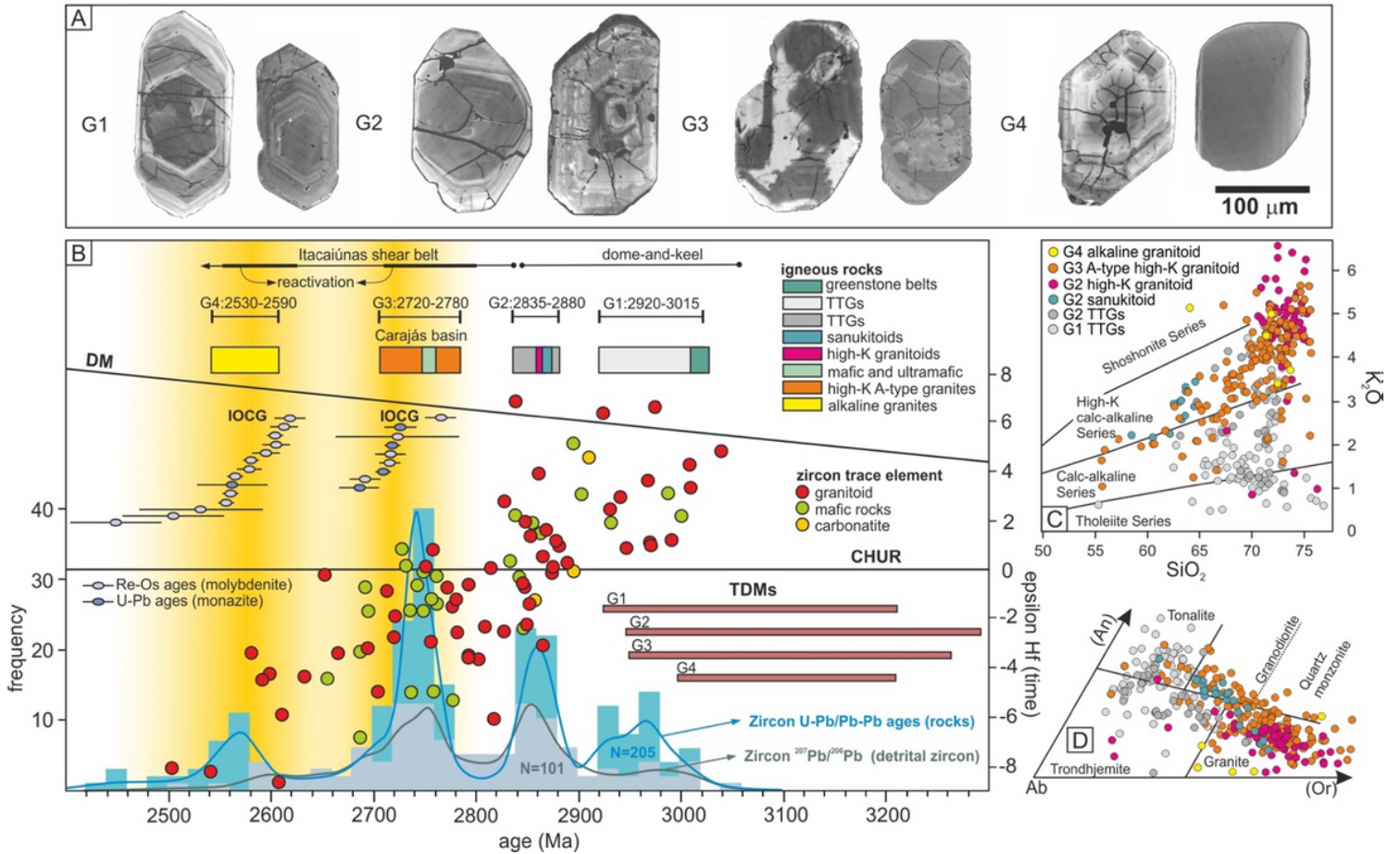


Figure 2

Distribution of U-Pb ages and Hf isotopic compositions of igneous rocks and detrital zircons from CMP. A. Representative cathodoluminescence images of detrital zircons of the four distinct groups of ages (G1-G4) from CMP modern drainages samples. B. Groups of ages G1 to G4 defined by the distribution of zircon U-Pb and Pb-Pb ages from exposed rocks (blue thick line) (N=238) and distribution of $^{207}\text{Pb}/^{206}\text{Pb}$ detrital zircon ages (green thick line) and zircon Hf isotopic compositions (N=102). TDM ages of each group are represented by the grey bars. Molybdenite Re-Os ages and monazite U-Pb ages of IOCG deposits from the CMP are reported in ref. [31]. C. K_2O vs SiO_2 diagram and subdivisions into different magmatic series showing progressive enrichment in K_2O from G1 to G4 granitoids. D. Albite-anorthite-orthoclase ternary diagram showing the predominance of tonalites and granodiorites for G1 and G2 and granites for G3 and G4.

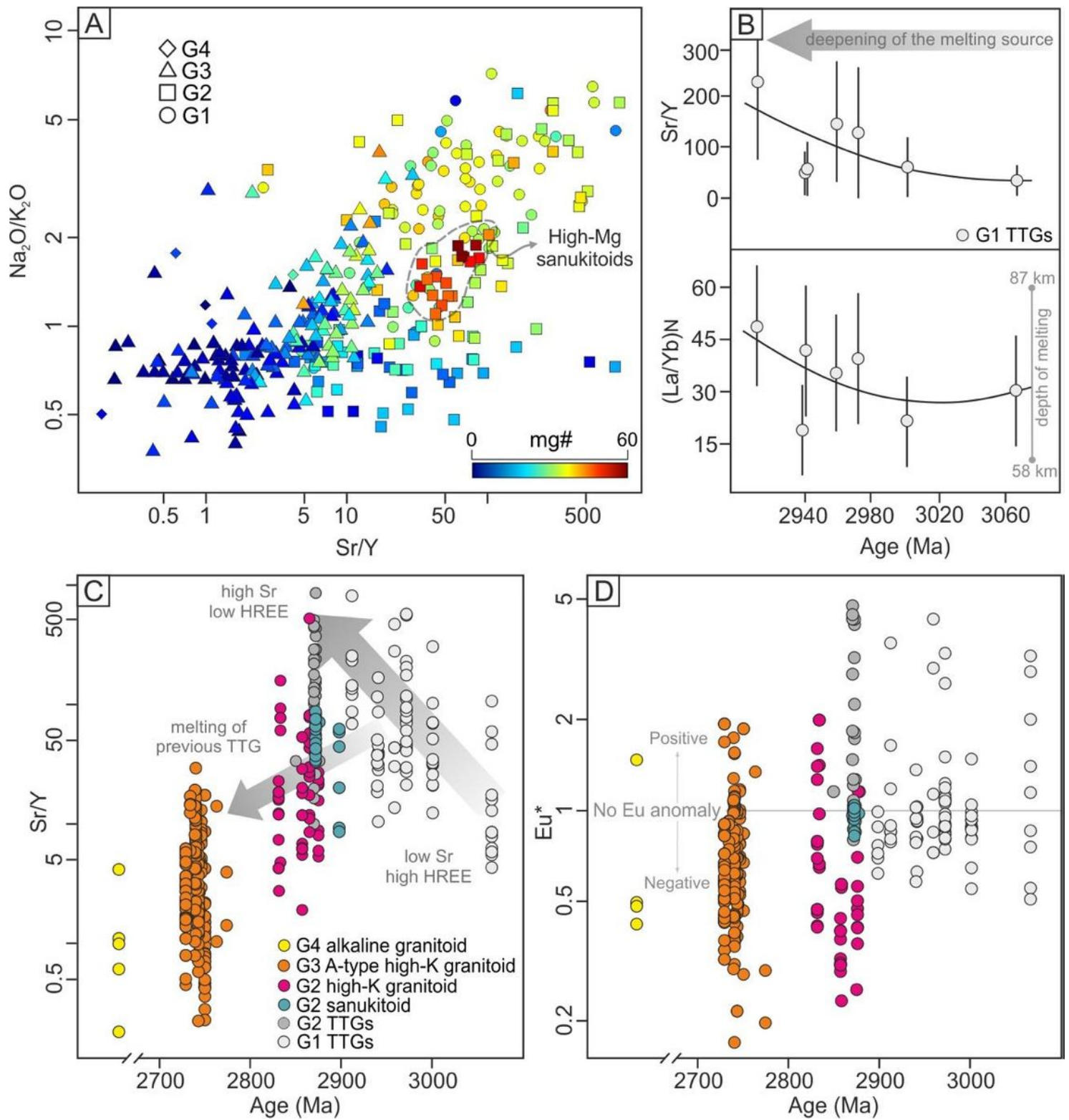


Figure 3

Geochemical variation of the CMP regional granitoid archive throughout time. A. Enrichment of K_2O over Na_2O accompanied by MgO and Sr/Y decrease over time. B. Variation of Sr/Y and $(\text{La}/\text{Yb})\text{N}$ for G1 TTGs over time (Ma) showing deepening of melt sources of the parent mafic rocks towards G2 granitoids. Depth (km) based on the $(\text{La}/\text{Yb})\text{N}$ based on ref. [46]. Error bars are 1σ standard deviation. C. Age of granitoids vs Sr/Y . D. Age of granitoids vs Eu^* .

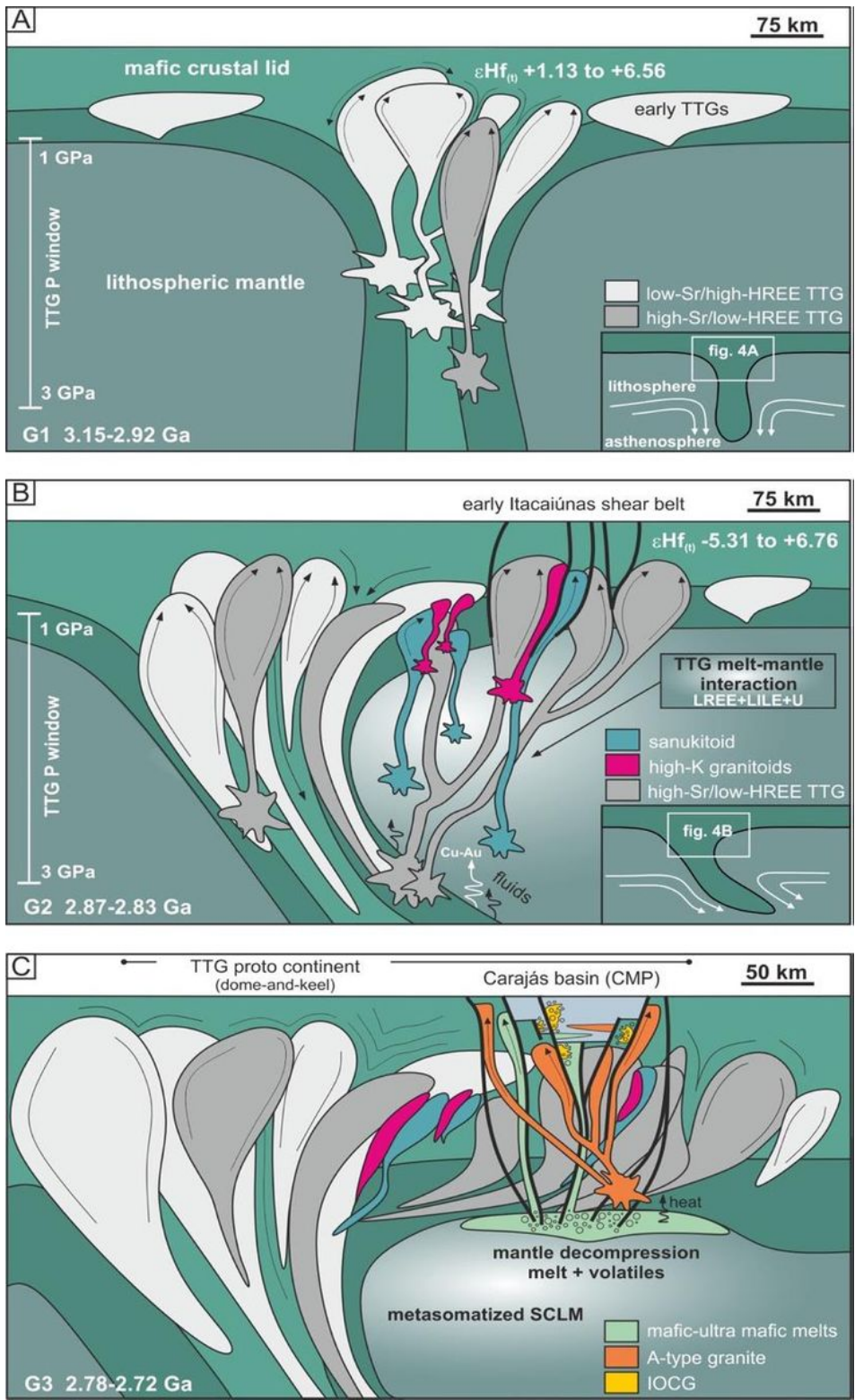


Figure 4

Transition from drip to plate tectonics and fertilization of the non-convective lithospheric mantle in the CMP. A. Foundering and melting of crustal mafic drips due to convection in the underlying asthenospheric mantle[4]. The drip includes juvenile basalt that melts at variable depths producing the juvenile G1 TTGs. Older shallower TTGs can also be produced at the base of the thick mafic crust[45]. B. With time and as a function of mantle convection and lid strength contrasts[31], the drip becomes asymmetric allowing for

increased variety in magma compositions in the G3 suites (2.87-2.83 Ga). Transitional TTGs form by mixing basalt-derived melts with anatexis of older TTGs in the drip. Drip asymmetry allows TTG melts to rise into and metasomatize the non-convective lithospheric mantle in LILE, REE and HFSE. Fluids released from the dehydrating crustal part of the drip promote partial melting of the previously metasomatized lithospheric mantle to form hot, high-Mg sanukitoids. These hot magmas rise to trigger minor melting of the TTG crust producing the high-K granitoids typically associated with sanukitoids. These magma suites are emplaced during the initial deformation of the Itacaiúnas shear belt. C. Lithospheric transtension at 2.78-2.72 Ga reactivates the Itacaiúnas shear belt to form the localized Carajás rift basin, promoting local mantle upwelling and decompression melting, generating mafic- ultramafic layered intrusions and basalts within the Carajás basin. The under- and intraplating of these mafic hot melts trigger the remelting of the TTG proto-crust to generate the A-type, high-K granitoids of G3. At this stage, the same drip- metasomatized non-convecting lithospheric mantle that previously produced sanukitoids releases fluids that use the translithospheric Itacaiúnas shear belt as conduits allowing them to reach shallower levels within the Carajás rift basin where they interact with basinal fluids[30] generating the first IOCG mineralization on Earth.

Supplementary Files

This is a list of supplementary files associated with this preprint. Click to download.

- [SupplementaryItemS1ZirconUPbLuHfandtraceelements.xlsx](#)
- [SupplementaryItemS2CompiledGeochemicaldata.xls](#)